

Faraday rotation study of NGC 612 (PKS 0131-36): a hybrid radio source and its magnetised circumgalactic environment

J. K. Banfield^{1,2}, S. P. O’Sullivan³, M. H. Wieringa⁴ and B. H. C. Emonts⁵

¹ *Research School of Astronomy and Astrophysics, Australian National University, Canberra, ACT 2611, Australia*

² *ARC Centre of Excellence for All-Sky Astrophysics (CAASTRO)*

³ *Hamburger Sternwarte, Universität Hamburg, Gojenbergsweg 112, Hamburg 21029, Germany*

⁴ *CSIRO Astronomy and Space Science, P.O. Box 76, Epping, NSW 1710, Australia*

⁵ *National Radio Astronomy Observatory, 520 Edgemont Road, Charlottesville, VA 22903*

Accepted 2018 November 11. Received 2018 October 22; in original form 2017 November 13.

ABSTRACT

We present a polarization and Faraday rotation study of the hybrid morphology radio galaxy NGC 612 (PKS 0131–36), using Australian Telescope Compact Array observations from 1 to 3 GHz. In general, the results are consistent with an external Faraday screen close to the radio source. In the eastern FRII lobe, the RM of the hotspot increases in magnitude towards the leading edge, as well as changing sign (compared to the rest of the lobe). The Faraday depolarization is also ~ 3 times larger at the hotspot than elsewhere. A plausible explanation for this is significant compression of ambient magnetised gas by the bow shock produced by the advancing hotspot. The western FRI lobe also exhibits some evidence of interaction with local magnetised gas, as a transverse band of high RM coincides with a distinct bend in the lobe. Previous observations of NGC 612 revealed an HI bridge of tidal debris along the direction of the eastern lobe towards the gas-rich companion NGC 619. We find no clear evidence that ionised gas associated with this bridge is either mixing with or lies in the foreground of the radio source. This is consistent with the absence of HI absorption against the hotspot, and indicates that the tidal debris must lie mostly behind the eastern lobe.

Key words: techniques: polarimetric – galaxies:active – galaxies: individual (NGC 612) – galaxies: interactions

1 INTRODUCTION

The nature of the interaction of radio-loud active galactic nuclei (AGN) with their environment is a key process in how both galaxies and radio-loud AGN evolve. The interaction between the radio lobes, formed by relativistic jets emanating from the supermassive black hole, with the interstellar medium (ISM), the intercluster medium (ICM), and the intergalactic medium (IGM), effect how gas is moved around to enhance or inhibit star formation.

Radio-loud AGN have been found to suppress star-formation and affect how the supermassive black hole and host galaxy co-evolve (i.e. Croton et al. 2006) while also providing mechanical heating to suppress the ICM cooling (i.e. McNamara & Nulsen 2012). Simulations by Mukherjee et al. (2016) of radio jets passing through a multi-phase ISM show that the low-power radio jets ($P_{\text{jet}} \leq 10^{43} \text{ ergs}^{-1}$) will impact the host galaxy over a larger volume than their high-power counterparts. Morganti et al. (2013) suggest that interactions between the radio-loud AGN jets with the ISM are most important in the young stages of the activity while at larger distances (10 – 100 kpc) the radio-loud AGN plays a ‘maintenance’ role.

On kpc scales, the impact of supersonic jets onto the ISM/IGM can create cocoons of (shocked) gas and synchrotron emission

with hotspot morphologies (FRII radio galaxies), while entrainment of gas by slow-jets can lead to bright radio sources with edge-darkened lobes (FRI radio galaxies). X-ray observations have shown radio emission and X-ray emission are anti-correlated in both galaxy groups and clusters (i.e. Carilli et al. 1994; Hardcastle et al. 2007). Croston et al. (2007, 2011) have also shown that shock heating from the radio-loud jets can affect environments in both massive galaxies and gas-rich mergers. This interplay between fuelling the AGN and the expansion of the radio-loud AGN into the ISM, IGM, and ICM can shape how galaxies evolve.

Studying the gas and magnetic field properties in and around radio lobes and jets provides key constraints on the details of the physical interaction between the radio jets and lobes with their environment. Saikia & Gupta (2003) suggest a link between the radio jets and the surrounding ISM through the differences of the degrees of polarization asymmetry between compact and extended radio sources. Radio continuum observations of the isolated radio galaxy B2 0755+37 by Guidetti et al. (2012) show anisotropic fluctuations of the rotation measure (RM) distribution across the two radio lobes consistent with cavities of thermal gas evacuated by the radio lobes.

The intrinsic magnetic field structure of radio lobes is typi-

arXiv:1811.06266v1 [astro-ph.HE] 15 Nov 2018

cally circumferential (i.e. parallel to the total intensity contours) at the edges of the lobes (Leahy et al. 1986). The jet magnetic field is typically longitudinal in powerful FRII type jets (Saikia & Salter 1988), while in FRI the inner part of the jet often has a longitudinal field before transitioning to a transverse field in the outer jet (Laing & Bridle 2014). High resolution studies of hotspots show a diverse range of structures that elude simple classification schemes, with similarly complicated behaviours in the associated polarization fraction and orientation (e.g. Black et al. 1992; Leahy et al. 1997). However, for those sources with an unambiguous ‘primary’ hotspot, the magnetic field is often approximately transverse to the observed (or inferred) jet direction, while a ‘secondary’, more diffuse, hotspot can often have a field transverse to a line connecting the hotspots (Hardcastle et al. 1997). This suggests the presence of significant field compression caused by, and aligned with, the shock front (e.g. Miller 1985).

The nearby powerful radio galaxy NGC 612 shows an apparent alignment between the radio-loud AGN and an HI bridge connected to a gas-rich companion (Emonts et al. 2008). Motivated by this, we observed NGC 612 in full polarization. Our goal is to examine the interaction between the radio-loud AGN and its gaseous environment, particularly at the hotspot. NGC 612 is a low redshift radio-loud AGN that allows for a detailed study of the environmental impact of radio-loud jets and lobes, which may be of additional use in interpreting the observed properties of high redshift systems.

NGC 612 is a typical S0 galaxy at $z = 0.0297$ (Westerlund & Smith 1966; Goss et al. 1980; Véron-Cetty & Véron 2001) hosting a radio-loud AGN PKS 0131-36 (Ekers et al. 1978). PKS 0131-36 has been classified as a HYbrid MOrphology Radio Source (HYMORS; Gopal-Krishna & Wiita 2000). The eastern radio lobe contains a hotspot near the furthest edge of the radio lobe typical of Fanaroff-Riley type II (FRII) radio sources (Fanaroff & Riley 1974). The western lobe shows no indication of a hotspot and is more diffuse, resembling FR type I (FRI) radio sources. Ekers et al. (1978) observed PKS 0131-36 at 1415 MHz with the Fleurs Synthesis Telescope and found that the monochromatic power across the whole radio extent of 400 kpc is $P_{1.4\text{GHz}} = 8.4 \times 10^{23} \text{ W Hz}^{-1} \text{ ster}^{-1}$ with a luminosity density of $L_{1.4\text{GHz}} = 1.6 \times 10^{31} \text{ W Hz}^{-1}$. Ekers et al. (1978) combined observations from the JVLA at 5 GHz with observations at 5 GHz and 8.1 GHz by Schilizzi (1976) to reveal a flat radio spectrum of the core that is compact at a limit of $< 0.3''$ centered on the host galaxy NGC 612.

Observations by Westerlund & Smith (1966) of NGC 612 reveal a dust disk and noted the similarity to Centaurus A. Ekers (1969) and Ekers et al. (1978) show that the radio axis is almost perpendicular to the dust disk at 78 degrees. Emission line measurements of [O II] $\lambda 3727$, [O III] $\lambda 4959$, 5007, and H α by Goss et al. (1980) uncovered a rotation curve out to approximately 40 kpc at a maximum rotational velocity of 340 km s^{-1} with the rotation axis being perpendicular to the dust disk. Further investigation by Holt et al. (2007) indicate the presence of a young stellar population of 0.04 to 0.1 Gyr throughout the stellar disk. Observations with *SUZAKU* from 0.5 – 60 keV by Eguchi et al. (2011) suggest NGC 612 is a Compton-thick AGN with $N_{\text{H}} \approx 10^{24} \text{ cm}^{-2}$ similar to a Seyfert Type 2 galaxy. The opening angle of NGC 612 was estimated by Eguchi et al. (2011) to be 60 – 70 degrees.

The combination of observations of X-ray, radio, and optical in the literature show evidence of a possibly interacting galaxy group. Westerlund & Smith (1966) determined there are 9 galaxies within $32'$ of NGC 612. HI observations by Emonts et al. (2008) reveal a faint HI bridge extending 400 kpc to nearby galaxy NGC 619 with no detectable optical counterpart related to the HI bridge

or tails. The HI mass distribution is mainly found in disks around NGC 619 ($M_{\text{HI}} = 8.9 \times 10^9 M_{\odot}$) and NGC 612 ($M_{\text{HI}} = 1.8 \times 10^9 M_{\odot}$), with $M_{\text{HI}} = 2.9 \times 10^8 M_{\odot}$ located in the HI bridge connecting the two galaxies (Emonts et al. 2008, see their Fig. 5). X-Ray observations by Tashiro et al. (2000) detect diffuse emission at 0.7 – 3 keV extending away from NGC 612 towards the eastern radio lobe and no emission near the western lobe. The hard X-Ray emission from 3 – 10 keV show a highly obscured active nucleus in NGC 612 (Tashiro et al. 2000).

In this paper, we present new broadband radio polarization and Faraday rotation observations of PKS 0131-36. We present our study as follows. Sections 2 and 3 provide details about the observations, calibration, and imaging of the radio data. Our analysis of these data are shown in section 4 with Section 5 providing the discussion. Throughout this paper we adopt a Λ CDM cosmology of $\Omega_M = 0.3$, $\Omega_{\Lambda} = 0.7$ with a Hubble constant of $H_0 = 70 \text{ km s}^{-1} \text{ Mpc}^{-1}$. At the redshift of NGC 612, $z = 0.0297$, the luminosity distance is $D_L = 130.1 \text{ Mpc}$ and the angular size distance is $D_A = 122.7 \text{ Mpc}$ giving a scale of $0.595 \text{ kpc arcsec}^{-1}$ (Wright 2006). We define the radio spectral index as $S_{\nu} \propto \nu^{\alpha}$.

2 OBSERVATIONS AND DATA PROCESSING

2.1 Synthesis Observations

The Australian Telescope Compact Array (ATCA; Frater et al. 1992) with the Compact Array Broadband Backend (CABB; Wilson et al. 2011) was used to produce a Stokes I and linear polarization mosaic of NGC 612 across the 16 cm CABB band. We used the first intermediate frequency (IF) band for continuum observations with $2049 \times 1 \text{ MHz}$ channels centered on the 16 cm CABB band.

Our observations were taken on 2012 October 25 – 26 for 13 hours in the 750B array configuration under project ID C2728. The shortest baseline is 61 m and the longest baseline is 4500 m. We used antenna 6 in our calibration. However, we removed antenna 6 for our analysis leaving the longest baseline at 765 m. The resulting angular resolution of our observations ranges from $92.86'' \times 31.90''$ (position angle = -10.6 deg) at 1.1 GHz to $26.37'' \times 14.82''$ (position angle = 0.8 deg) at 3 GHz. The primary beam full-width half-power (FWHP) ranges from $42'$ at 1.1 GHz to $15'$ at 3.1 GHz. A two pointing mosaic was made with one pointing centered on the East lobe of NGC 612 and a second pointing centered on the West lobe. This was done because the bright outer edges of the radio galaxy ($\sim 13'$ angular size) extend close to the FWHP at the highest frequencies. The mosaic also helped minimise the effect of instrumental polarization across the extent of the source. At the time of our observations the instrumental polarization response was unknown across the 16 cm CABB band both in frequency and distance from the pointing center.

The primary flux calibrator, PKS 1934–638 (14.95 Jy at 1.380 GHz; Reynolds 1994), was observed twice during the observations. We observed B0048–427 as the phase calibrator for two minutes once every hour.

2.2 Calibration

Calibration and editing of the uv -data was completed in MIRIAD¹ version 1.5 (Sault et al. 1995). The data were loaded into MIRIAD

¹ <http://www.atnf.csiro.au/computing/software/miriad/>

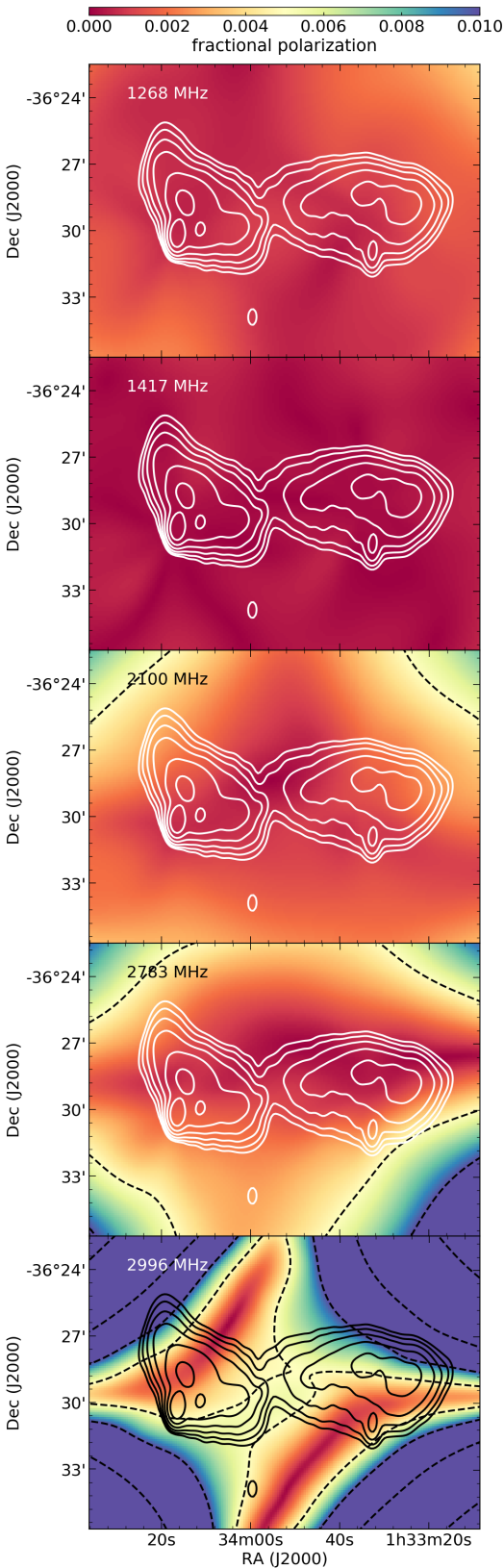


Figure 1. The instrumental polarization response (colorscale) of the ATCA across the 16 cm CABB band for our observations as described in Section 2.3. The dashed contours mark the 0.5, 1, and 5 per cent instrumental polarization. The Stokes I data of NGC 612 are shown with the solid contours, starting at $4\sigma_1$ and increasing by a factor of 2. A color version of this figure is available online.

using the task `atlod` (v.1.52) and flagging of known radio frequency interference (RFI) was applied using the option `birdie`. The bandpass was calibrated with PKS 1934–638 using `mfcal` (v.1.17). The frequency dependent gain and polarization leakage was solved for using the task `gpca1` (v.1.22) in 8 bins of 256 MHz (using the parameter `nfbn=8`). The bandpass and leakage solutions were then copied to the secondary calibrator B0048–427 using `gpcopy` (v.1.12). The secondary was used to solve for the complex antenna gains as a function of time and for the polarization of the secondary, again in 8 frequency bins, using `gpca1` (see Schnitzeler et al. 2013). We then used task `gpboot` to perform absolute flux calibration by scaling the secondary gains to those determined on the primary calibrator and used task `mfboot` to correct any remaining error in the spectral slope. We expect the resulting flux density scale to be accurate to better than 5% across the frequency band. Automated flagging of the calibrators was completed using `pgflag` (v.1.30), the automatic flagging routine developed by Offringa et al. (2010) and incorporated into the MIRIAD software package. Manual flagging of the calibrators was also completed using `uvflag` (v.1.7). Once the calibration was complete, we copied the solutions to NGC 612. We then flagged NGC 612 using `pgflag` and manually flagged with `uvflag`. After flagging, the useable data were between 1.2 – 3.0 GHz.

2.3 Instrumental Polarization

The main goal of our observations is to examine the rotation measure and possible interaction of the radio lobes of NGC 612 with the environment. In order to accurately test our hypothesis, we require measurements of the instrumental polarization response across the 16 cm CABB band. We present our analysis in Figure 1 for five different frequencies (1268, 1417, 2100, 2783, and 2996 MHz) with respect to our observations of NGC 612. The instrumental polarization maps were created using the off-axis observations of PKS 1934–638 by J. Stevens from 2011². We synthesised observations using the MIRIAD task `offpol` (v.1.8) with the new beam data assuming 12 hour observations with an hour angle range of -6 h to $+6$ h for each mosaic pointing for each of the five different frequencies in Stokes I , Q , and U . The resulting images were mosaicked together using `linmos` (v.1.32) and combined together to evaluate the fractional polarization at each frequency.

We found that the instrumental polarization response increases with frequency across the 16 cm CABB band. At 1268 MHz, the fractional polarization is below 0.004 across the primary beam. At the higher end of the band, the instrumental fractional polarization increases to 0.05 well within the primary beam. In Figure 1 we overlay the Stokes I flux density contours of NGC 612 starting at the $4\sigma_1$ level and increasing by a factor of 2. At the low end of the band, there is less than 0.3 per cent instrumental polarization across NGC 612. In the middle of the band, the response increases to 0.5 per cent near the radio lobe edges of NGC 612. At the top end of the band (2996 MHz), the instrumental polarization does not exceed 2 per cent across NGC 612 with the highest polarization leakage near the radio lobe edges. These maps are used in Section 4.2 to provide an additional systematic uncertainty when modelling the fractional polarization across the 16 cm band.

² http://www.narrabri.atnf.csiro.au/people/ste616/beamshapes/beamshape_16cm.html

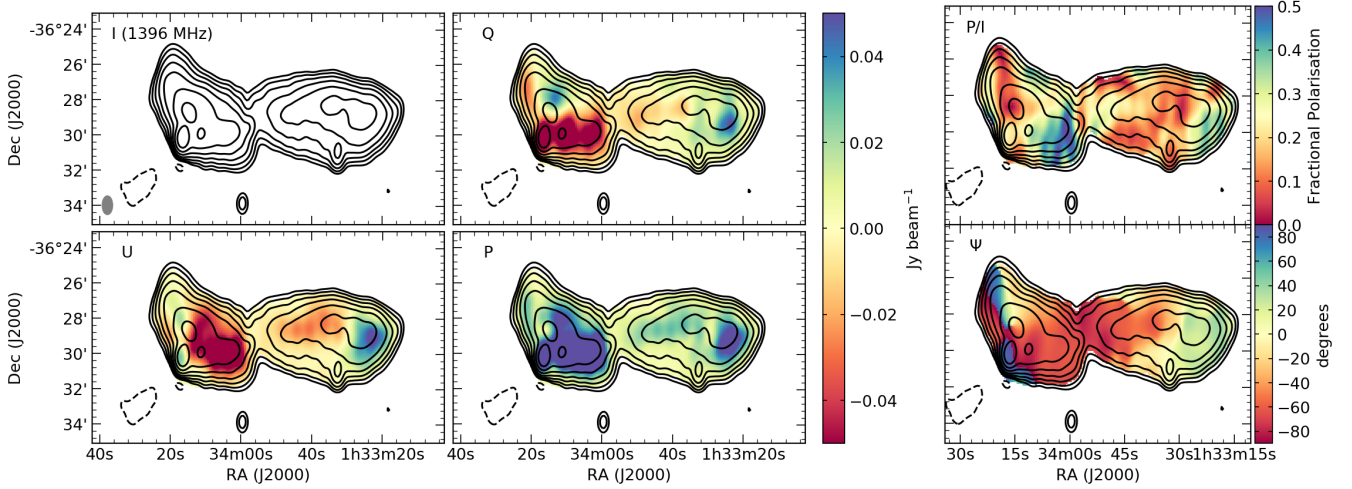


Figure 2. The full Stokes (I , Q , U , P) images with polarization angle (Ψ) and fractional polarization (P/I) images at 1396 MHz. The black contours are the Stokes I radio emission from the full band continuum image with dashed contours at $-2\sigma_1$ and solid contours at $2\sigma_1$ and then increasing by factors of 2. The grey oval in the lower left of the Stokes I image represents the beam. A color version of this figure is available online.

3 IMAGES

3.1 Total Intensity

Large fractional bandwidth poses three problems with wide-band wide-field imaging as noted by Condon et al. (2012): (1) the field of view; (2) the point spread function; and (3) the flux densities of sources can vary significantly with frequency. The fractional bandwidth of the 1.1 – 3.1 GHz CABB band is 95 per cent and if we image the full band at once we would encounter the above imaging issues. We also encountered an additional issue with respect to our target source NGC 612. The radio lobes of NGC 612 are well resolved and show complex structure at all spatial resolutions. As a result, we took extra steps in imaging both in both continuum and linear polarization to decrease calibration and imaging artefacts.

We used only antenna 6 baselines for the first rounds of phase self calibration, suppressing the resolved structure of the radio lobes and leaving the compact regions. We then excluded the antenna 6 data from further processing. For the second stage of imaging we used all 10 remaining baselines, but excluded the shortest two baselines in the self calibration. We carefully masked the emission regions to avoid sidelobes in the model. The Stokes I continuum image was imaged in 3×683 MHz bands, a compromise between limiting the fractional bandwidth to avoid deconvolution errors and retaining enough data for good imaging. The flux density variations of the source were handled with MFS imaging and deconvolution using MIRIAD tasks `invert` (v.1.22, with options `mfs` and `sdb`) and `mfclean` (v.1.11) to model the flux and spectral index in each of the three 683 MHz bands. The three frequency bands were convolved to the lowest resolution and combined in the image plane using `linmos`. The final beam size is $58.8'' \times 31.0''$ at -0.75 degrees. The resulting Stokes I noise level of $\sigma_1 = 1.59$ mJy beam $^{-1}$, is ~ 10 times larger than the theoretical thermal noise level, indicating that the image dynamic range is limited by calibration and imaging errors and not thermal noise.

3.2 Polarization

We split the band into 16×128 MHz bands to image polarization across the source. Each 128 MHz band was imaged separately and then convolved to the lowest resolution of $78'' \times 35''$ at -1 degree. Adopting the same notation and procedure as Sokoloff et al. (1998), Farnsworth et al. (2011) and O’Sullivan et al. (2012) we define the complex linear polarization as:

$$P = Q + iU = pIe^{2i\Psi} = pIe^{2i(\Psi_0 + \text{RM}\lambda^2)}, \quad (1)$$

where Ψ is the observed polarization angle and I , Q , and U are the measured Stokes parameters. The fractional polarization is defined as:

$$p = \sqrt{q^2 + u^2}, \quad (2)$$

where $q = Q/I$ and $u = U/I$. The linear polarization angle is

$$\Psi = \frac{1}{2} \arctan \frac{u}{q}. \quad (3)$$

The Faraday rotation measure (RM) rotates the linear polarization angle from its intrinsic value (Ψ_0) as a function of wavelength-squared (λ^2). The amount of Faraday rotation depends on the properties of magnetised plasma along the line of sight, as $\text{RM} \sim 0.81 \int_L n_e B_{\parallel} dl$ with n_e being the free electron number density (in cm^{-3}), B_{\parallel} the line-of-sight magnetic field strength (in μG) and L the total path length (in parsecs).

Figure 2 shows the full Stokes (I , Q , U , P) images with polarization angle (Ψ) and fractional polarization (P/I) images at 1396 MHz. The black contours are the Stokes I radio emission from the full band continuum image starting at $4\sigma_1$ and increasing by a factor of 2. Imaging using multi-frequency synthesis to better fill the uv -plane and obtaining the largest range in RM (by imaging in narrow frequency ranges) are opposing constraints. We attempted imaging 32, 64, 128 and 256 MHz band images and found that below 128 MHz the images were dominated by deconvolution errors resulting from insufficient uv -coverage to image the complex structure of the radio lobes of NGC612. Therefore we decided on 128 MHz as the best frequency resolution we can achieve with this data. This provided a nominal RM resolution of ≈ 76 rad m^{-2} and

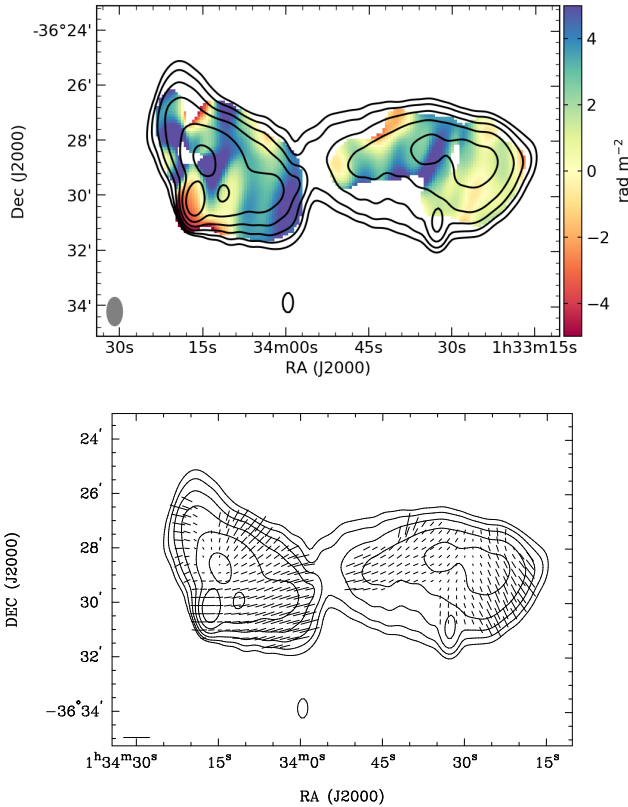


Figure 3. Top: The RM distribution of NGC 612 in rad m^{-2} . The solid black contours show the Stokes I emission starting at $4\sigma_I$ and increasing by factors of 2. The synthesised beam is shown in the bottom left corner of the image. Bottom: Intrinsic polarization angle (Ψ_0) map after correction for Faraday rotation. The vectors represent the orientation of Ψ_0 with the length corresponding to the relative fractional polarization. A vector length corresponding to a fractional polarization of 1 is shown in the bottom left corner of the image. A colour version of this figure is available online.

a maximum detectable RM of $\approx 370 \text{ rad m}^{-2}$. In this case, bandwidth depolarization caused by averaging over 128 MHz is negligible considering the mean RM of $\approx 2 \text{ rad m}^{-2}$ in the direction of this source.

4 ANALYSIS

4.1 Rotation Measure

Faraday rotation provides information on the magnetic field strength and geometry and ionized particle distributions of magnetised thermal material along the line of sight. Complicated Faraday structures can exist in both compact radio sources (i.e. O’Sullivan et al. 2012) and from diffuse radio emission found in the lobes of radio sources (i.e. Guidetti et al. 2012). The origin of such RM complexity is still under debate, but it is expected that RM variations caused by the local source environment are a key factor (e.g. O’Sullivan et al. 2017; Anderson et al. 2018). One can potentially use the RM to determine the type of interaction between the radio lobe plasma and the external medium and constrain the magnetic field properties of the intergalactic gas (e.g. Laing et al. 2008; Guidetti et al. 2011). To determine the distribution of polarization and RM across the lobes, we applied the technique of RM synthesis

(Brentjens & de Bruyn (2005) on the 16 x 128 MHz images (Section 3.2).

The RM distribution, shown in Figure 3, was produced from the fractional Q and U data and pixels were blanked where the peak polarized intensity was less than $8\sigma_{QU}$ (where σ_{QU} was determined from the Q and U RM synthesis spectrum far from the peak). The mean RM of the eastern lobe is $+2.6 \text{ rad m}^{-2}$ with a standard deviation of 2.6 rad m^{-2} . However, the RM is negative at the hotspot and increases in magnitude towards the leading edge (from -1.8 rad m^{-2} to -5 rad m^{-2}). Figure 4 shows the behaviour of the polarization data at the hotspot, with the RM of $-1.8 \pm 0.1 \text{ rad m}^{-2}$ overlaid on the data in the angle versus wavelength-squared panel. For the western lobe, the mean and standard deviation in RM are $+1.7 \text{ rad m}^{-2}$ and 1.8 rad m^{-2} , respectively. The RM increases along the ridge from $\sim 0 \text{ rad m}^{-2}$ in the inner lobe to $\sim 5 \text{ rad m}^{-2}$ at the bend and back down to $\sim 1 \text{ rad m}^{-2}$ towards the end point of the lobe. The mean RM error is 0.3 rad m^{-2} .

4.2 Depolarization

The high fractional polarization observed across the lobes in the 16 cm band, with a mean of 0.23 and a standard deviation of 0.11, is consistent with the small RM variations observed across the majority of the lobes on scales larger than the synthesised beam (Section 4.1). However, there are significant variations in the fractional polarization with frequency in particular locations, indicating substantial RM variations on smaller scales (e.g. Figure 4).

To better quantify these variations, we parameterise the depolarization across the radio lobes of NGC 612 using the Burn law (Burn 1966), which is also commonly known as external Faraday dispersion (Sokoloff et al. 1998). We follow a procedure similar to that described in Laing et al. (2008), where we fit the observed data with the relation

$$\ln p(\lambda) = \ln p(0) - k\lambda^4, \quad (4)$$

where λ is the wavelength (m) of our observations, k is the depolarization parameter, and $p(0)$ is the intrinsic polarization. Figure 6 shows the fit for the hotspot. We only use those pixels where $\sigma_p > 4$ in all frequencies and include an additional systematic error based on a linear interpolation of the widefield instrumental polarization maps (Section 2.3). We plot the Burn k parameter and the intrinsic polarization maps in Figure 5, along with their corresponding formal error maps.

The observed depolarization differs significantly between the two radio lobes. The eastern FR II radio lobe has a mean k value of $100 \text{ rad}^2 \text{ m}^{-4}$ with a standard deviation of $124 \text{ rad}^2 \text{ m}^{-4}$ and a mean error of $70 \text{ rad}^2 \text{ m}^{-4}$. At the location of the hotspot $k = 124 \pm 8 \text{ rad}^2 \text{ m}^{-4}$ indicating significant depolarization, while k decreases upstream towards the host galaxy without much evidence for large depolarization (typical values of $k \sim 40 \text{ rad}^2 \text{ m}^{-4}$ with errors of $\sim 30 \text{ rad}^2 \text{ m}^{-4}$). The western FR I radio lobe shows evidence for a banded depolarization and repolarization structure along the radio lobe, however the significance of the variations are low. The mean k value of $70 \text{ rad}^2 \text{ m}^{-4}$ is lower than the eastern lobe, but the standard deviation is higher at $160 \text{ rad}^2 \text{ m}^{-4}$. The large mean error in k of $100 \text{ rad}^2 \text{ m}^{-4}$ means that these variations are significant at about a 90% confidence level. However, there is also an east-west ripple pattern visible in the total intensity, so these variations could be related to imaging artefacts. In general, there appears to be more complex polarization behaviour than described by the Burn law, and more detailed modelling of the radio lobes (e.g. Kaczmarek

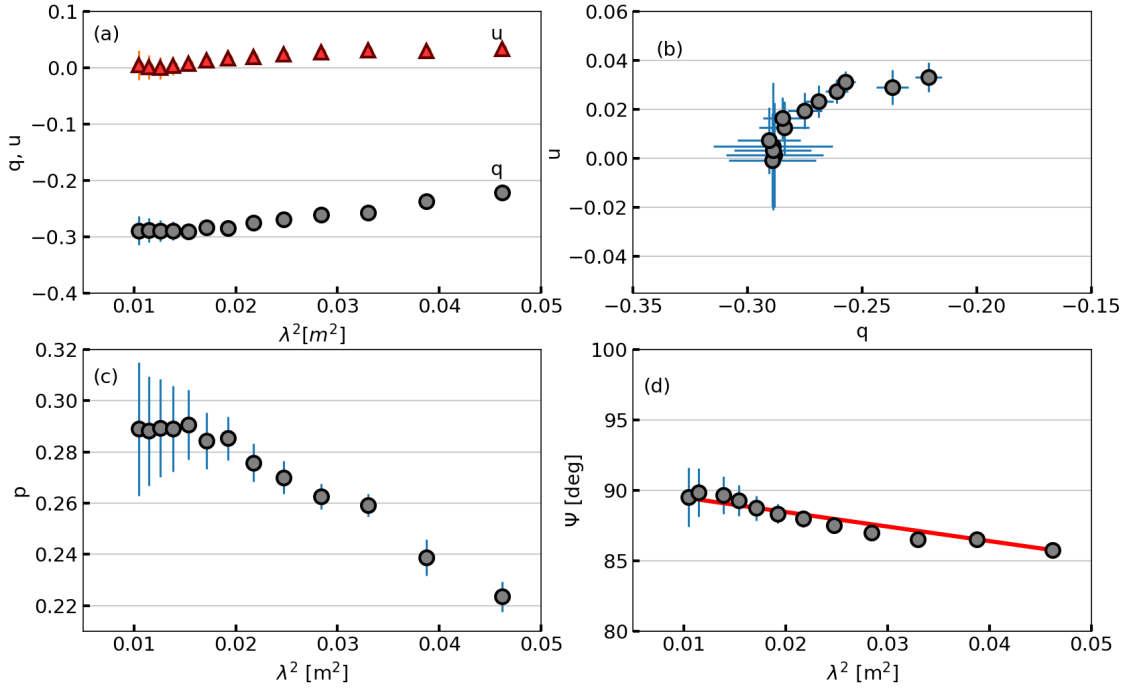


Figure 4. The polarization data at the location of the hotspot. (a) q and u as a function of wavelength squared. (b) q versus u . (c) Fractional polarization versus wavelength squared. (d) Polarization angle versus wavelength squared, overlaid with a red solid line corresponding to an RM of -1.8 rad m^{-2} , as derived from RM synthesis at that location (Figure 3). A color version of this figure is available online.

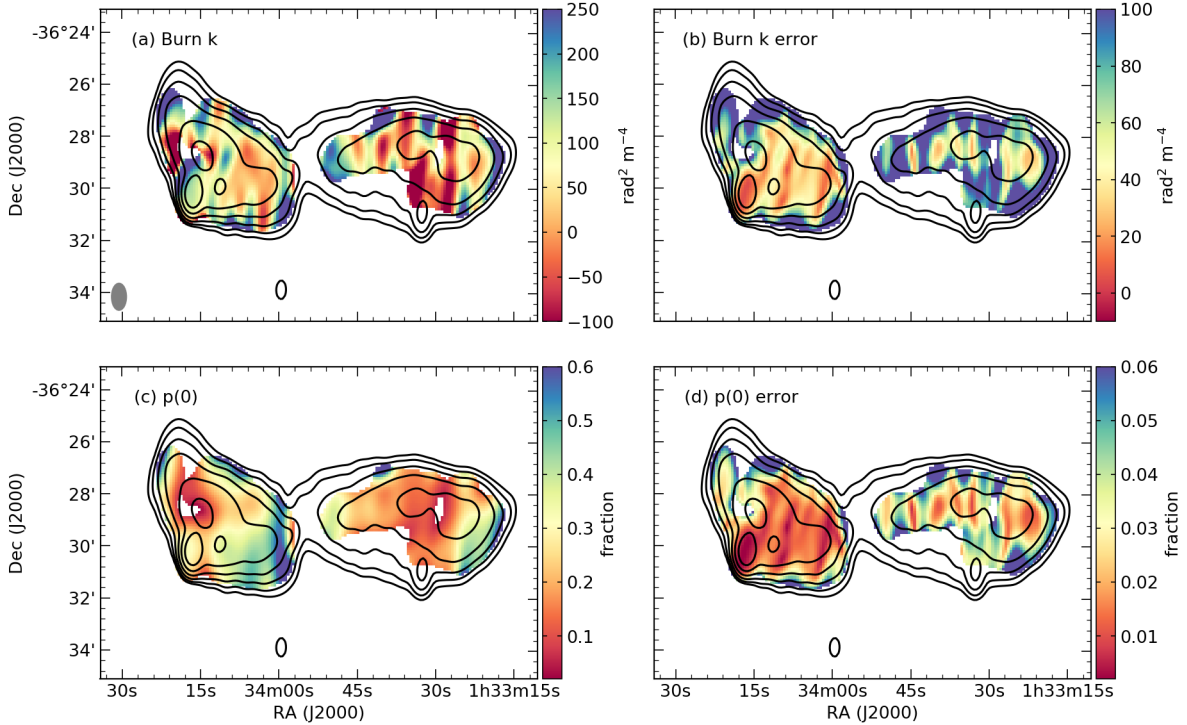


Figure 5. Representation of the depolarization of NGC 612 using the Burn law (Section 4.2). (a) The fitted depolarization parameter k from the Burn law. (b) The error in k . (c) The intrinsic polarization $p(0)$ from the extrapolation of the Burn law to zero wavelength. (d) The error in $p(0)$. The grey oval in the lower left of (a) represents the beam of the Stokes I emission shown with the black contours. The contours start at $4\sigma_1$ and increase by a factor of 2. A color version of this figure is available online.

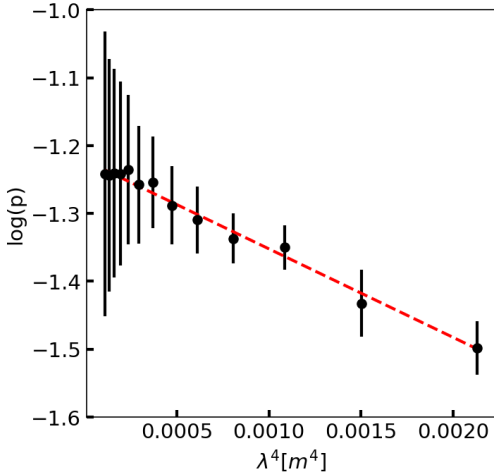


Figure 6. Plot of the natural log of the fractional polarization p versus λ^4 . The dashed red line represents the best fitting slope of $k = 124 \pm 8 \text{ rad}^2 \text{ m}^{-4}$. A color version of this figure is available online.

et al. 2018) with higher sensitivity and importantly, higher fidelity observations being required to investigate this further.

At the hotspot, $p(0) = 0.295 \pm 0.003$, and the mean value of $p(0)$ across the eastern lobe is ~ 0.3 with a standard deviation of 0.15, while the mean error is ~ 0.03 . This is comparable to the $p(0)$ mean and standard deviation of 0.24 and 0.14, respectively, of the western lobe (with a mean error of ~ 0.04). The intrinsic fractional polarization increases to as much as 0.7, close to the theoretical maximum, at the lobe edges (albeit with relatively large errors of ~ 0.1). In Figure 3 (bottom), we show the intrinsic polarization angle (Ψ_0) map, after correction for Faraday rotation, and with the polarization vectors scaled by the intrinsic fractional polarization. The Ψ_0 distribution implies a circumferential magnetic field at the edges of the radio lobes, as is commonly observed (e.g. Leahy et al. 1986). The southern edge of the eastern lobe is an exception to this, with a magnetic field perpendicular to the total intensity contour lines. The field in the central lobe regions is orientated approximately along the ridge axes, with this alignment maintained even through the significant bend in the western lobe. The field orientation at the hotspot is not exactly perpendicular to the presumed jet direction, although observations at higher angular resolution that resolve the hotspot region are needed for further study.

5 DISCUSSION

Here we discuss the polarization and Faraday rotation properties of NGC 612 in relation to the details of the interaction between this hybrid morphology radio source and the gas in the circumgalactic environment. Large scale mixing of ionized thermal material with the relativistic material in the radio lobe would produce internal Faraday rotation (e.g. Cioffi & Jones 1980). This effect has a unique RM and depolarization signature, for sufficient wavelength coverage, that can be detected using RM synthesis as well as through detailed modelling of the variation in both the polarization angle and amplitude with wavelength squared (e.g. Anderson et al. 2018). We find no clear evidence for internal Faraday rotation in either lobe from the current data, although the western lobe does show a complex depolarization structure that should be investigated further with higher fidelity observations, such as those that will

be attained by the Australian Square Kilometre Array Pathfinder (ASKAP; Johnston et al. 2009).

In the case of the circumgalactic gas mixing at the lobe boundary rather than mixing throughout the lobe volume, then the RM structure is also expected to be correlated with the source structure. For example, Bicknell et al. (1990) considered a model where any emission from the boundary layer is completely depolarized and the RM structure correlates with the lobe structure without any large variation in the degree of polarization with wavelength. The western lobe shows a significant increase in RM magnitude at the location of a distinct bend in the lobe. This suggests that the ambient gas responsible for the observed Faraday rotation is in the local source environment and being influenced by the radio lobe. However, an RM structure correlated with the source structure does not directly imply a mixing layer. Recently, Guidetti et al. (2012) discovered coherent RM structures across the lobes of several nearby radio galaxies. They postulated that these could be potentially generated by compression along with draping and stretching of the magnetic field in the ambient gas by the expansion of the lobes (e.g. Dursi & Pfrommer 2008).

In the case of the eastern lobe, the strong shock expected at the hotspot should compress the ambient gas, enhancing the RM contribution local to the source, if the external medium is appreciably magnetised (e.g. Carilli et al. 1988). We consider the bow-shock scenario as a possible explanation for the RM structure of the hotspot, where the RM magnitude increases across the hotspot towards the leading edge of the lobe. The amount of depolarization at the hotspot is also ~ 3 times higher than along the ridge of the lobe. The increase in depolarization makes sense if the magnetic field in the compressed external medium is tangled on scales $\ll 50$ kpc. The negative sign of the RM at the hotspot is opposite to the positive RM across the majority of the eastern lobe, also consistent with a significant influence of the radio lobe on the external medium at this location.

Interestingly, NGC 612 is connected to NGC 619 through a narrow bridge of tidal debris detected in HI (Emonts et al. 2008). The HI bridge connects these two galaxies along the Eastern radio lobe. From an in-depth study of both the HI bridge and the regularly rotating HI disk around HGC 612, Emonts et al. (2008) argue that the bridge is the result of an interaction or collision between NGC 612 and NGC 619 that occurred at least a Gyr ago. Figure 7 visualizes the faint HI emission from the bridge in relation to the Eastern FR II radio lobe and the hotspot. It is likely that the majority of the HI emitting material is located behind the radio source. If it were in front of the radio emission, we would have observed the HI gas in the line of sight towards the radio hotspot in absorption rather than emission.

The presence of an HI bridge indicates that there is likely a larger reservoir of tidal debris between NGC 612 and NGC 619. If part of this tidal debris was shock ionised by the expanding radio lobe, and in the foreground, then there should be a signature of this ionised gas in the Faraday rotation and depolarization maps. Figure 7(b) and (c) shows a zoom-in of the hotspot region with the HI contours overlaid on the RM map and depolarization map, respectively. As there is no clear correspondence, we can conclude that any significantly ionised tidal debris is located behind the radio lobe, consistent with the eastern jet and radio lobe orientated either close to the plane of the sky or towards the line of sight. While we cannot rule out an interaction between the radio lobe and the tidal debris, the RM properties discussed in this paper, combined with the fact that the HI in the bridge has a very narrow velocity dispersion (Emonts et al. 2008), provide no clear evidence for this.

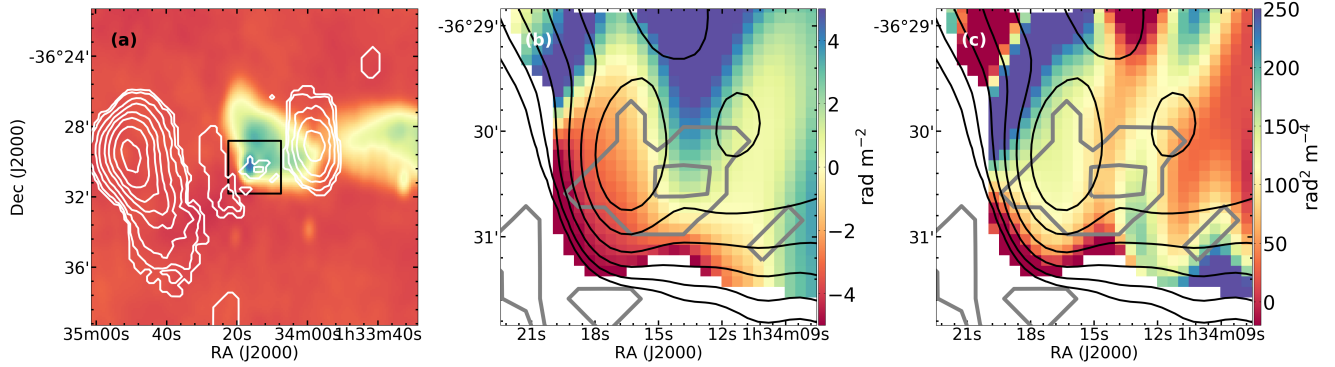


Figure 7. The HI emission from Emonts et al. (2008) in relation to the radio continuum emission of NGC 612. (a) Contours of the HI emission in and between NGC 612 and NGC 619 overlaid into the Stokes I continuum emission. Contour levels: 0.05, 0.14, 0.24, 0.4, 0.6, 0.9, 1.2, 1.6, 2.0 $\text{Jy beam}^{-1} \times \text{km s}^{-1}$. The HI emission in the bridge is faint and difficult to accurately image in this total intensity plot, but it shows up as a distinct feature in the position-velocity maps of Emonts et al. (2008). The background color image is the Stokes I continuum image. The black square indicates the zoomed-in region of the (b) and (c) panels. (b) The background color image shows the RM map with HI emission in grey contours and Stokes I emission in black contours. (c) Similar to (b) with the colormap now showing the Burn law k parameter representing Faraday depolarization. A color version of this figure is available online.

Deeper HI studies in combination with X-ray and $\text{H}\alpha$ observations would help further illuminate the complex gas dynamics of this system.

6 SUMMARY

We have presented an analysis of the interaction between the lobes of the hybrid morphology radio galaxy, NGC 612, and the circumgalactic gas, through a broadband radio polarization and Faraday rotation study, using the Australian Telescope Compact Array at 1 to 3 GHz. Previous HI observations revealed the presence of a bridge of tidal debris connecting NGC 612 to a nearby galaxy. The tidal bridge is coincident on the sky with the eastern FRII lobe, with no HI detected towards the western FRI lobe.

We examined the linear polarization, Faraday rotation and depolarization distributions, finding that they are consistent with external Faraday rotation caused by a turbulent magnetic field in the intragroup medium. There is evidence for a correlation between the Faraday structure and the radio morphology, both at the location of the hotspot in the eastern lobe and at a bend in the western lobe. In particular, the enhancement in RM and depolarisation at the hotspot can be plausibly explained by the projection of part of the bow-shock region onto the lobe, where the ambient gas has been appreciably compressed. Although several aspects of the RM and depolarization structure suggest an influence of the radio galaxy on the ambient magnetoionic environment, there is no evidence for either large scale mixing of the eastern radio lobe with the gas in the HI bridge, or large amounts of ionised debris in the foreground of the radio lobe.

After correction for the effect of Faraday rotation, we find a mainly circumferential intrinsic magnetic field structure of the lobes (the southern edge of the eastern lobe is a notable exception to this). This is a commonly observed feature of double-lobed radio sources, and is consistent with an initially tangled magnetic field that is stretched by the shearing motion along the direction of the backflow, in addition to outward compression due to the lobe expansion.

In general, broadband radio polarization observations with higher image fidelity and sensitivity are required to better determine the nature of the relationship between the Faraday rotating

gas and the radio lobe. Complementary $\text{H}\alpha$ and X-ray observations would also provide a better understanding of the multi-phase intragroup medium surrounding this hybrid morphology radio galaxy. In general, this work demonstrates some aspects of how broadband radio polarization data can provide a means to examine the detailed role of AGN feedback in environments other than galaxy clusters at low redshift. Further studies of NGC 612 and other galaxies in similar environments can provide new insights into radio galaxy evolution and feedback across a wide range of redshifts.

ACKNOWLEDGMENTS

We would like to thank R. Ekers for useful comments and discussion. Parts of this research were conducted by the Australian Research Council Centre of Excellence for All-sky Astrophysics (CAASTRO), through project number CE110001020. The Australia Telescope Compact Array is part of the Australia Telescope, which is funded by the Commonwealth of Australia for operation as a National Facility managed by CSIRO. The National Radio Astronomy Observatory is a facility of the National Science Foundation operated under cooperative agreement by Associated Universities, Inc. The figures in this work made use of Astropy, a community-developed core Python package for Astronomy (Astropy Collaboration et al. 2013). SPO acknowledges financial support from the Deutsche Forschungsgemeinschaft (DFG) under grant BR2026/23.

REFERENCES

- Anderson C. S., Gaensler B. M., Heald G. H., O’Sullivan S. P., Kaczmarek J. F., Feain I. J., 2018, *ApJ*, **855**, 41
- Astropy Collaboration et al., 2013, *A&A*, **558**, A33
- Bicknell G. V., Cameron R. A., Gingold R. A., 1990, *ApJ*, **357**, 373
- Black A. R. S., Baum S. A., Leahy J. P., Perley R. A., Riley J. M., Scheuer P. A. G., 1992, *MNRAS*, **256**, 186
- Brentjens M. A., de Bruyn A. G., 2005, *A&A*, **441**, 1217
- Burn B. J., 1966, *MNRAS*, **133**, 67
- Carilli C. L., Perley R. A., Dreher J. H., 1988, *ApJ*, **334**, L73
- Carilli C. L., Perley R. A., Harris D. E., 1994, *MNRAS*, **270**, 173
- Cioffi D. F., Jones T. W., 1980, *AJ*, **85**, 368

- Condon J. J., et al., 2012, *ApJ*, **758**, 23
- Croston J. H., Kraft R. P., Hardcastle M. J., 2007, *ApJ*, **660**, 191
- Croston J. H., Hardcastle M. J., Mingo B., Evans D. A., Dicken D., Morganti R., Tadhunter C. N., 2011, *ApJ*, **734**, L28
- Croton D. J., et al., 2006, *MNRAS*, **365**, 11
- Dursi L. J., Pfrommer C., 2008, *ApJ*, **677**, 993
- Eguchi S., Ueda Y., Awaki H., Aird J., Terashima Y., Mushotzky R., 2011, *ApJ*, **729**, 31
- Ekers R. D., 1969, Australian Journal of Physics Astrophysical Supplement, **6**, 3
- Ekers R. D., Goss W. M., Kotanyi C. G., Skellern D. J., 1978, *A&A*, **69**, L21
- Emonts B. H. C., Morganti R., Oosterloo T. A., Holt J., Tadhunter C. N., van der Hulst J. M., Ojha R., Sadler E. M., 2008, *MNRAS*, **387**, 197
- Emonts B. H. C., et al., 2010, *MNRAS*, **406**, 987
- Fanaroff B. L., Riley J. M., 1974, *MNRAS*, **167**, 31P
- Farnsworth D., Rudnick L., Brown S., 2011, *AJ*, **141**, 191
- Frazer R. H., Brooks J. W., Whiteoak J. B., 1992, Journal of Electrical and Electronics Engineering Australia, **12**, 103
- Gopal-Krishna Wiita P. J., 2000, *A&A*, **363**, 507
- Goss W. M., Danziger I. J., Fosbury R. A. E., Boksenberg A., 1980, *MNRAS*, **190**, 23P
- Guidetti D., Laing R. A., Croston J. H., Bridle A. H., Parma P., 2012, *MNRAS*, **423**, 1335
- Guidetti D., Laing R. A., Bridle A. H., Parma P., Gregorini L., 2011, *MNRAS*, **413**, 2525
- Hardcastle M. J., Alexander P., Pooley G. G., Riley J. M., 1997, *MNRAS*, **288**, 859
- Hardcastle M. J., Kraft R. P., Worrall D. M., Croston J. H., Evans D. A., Birkinshaw M., Murray S. S., 2007, *ApJ*, **662**, 166
- Holt J., Tadhunter C. N., González Delgado R. M., Inskip K. J., Rodriguez Zaurin J., Emonts B. H. C., Morganti R., Wills K. A., 2007, *MNRAS*, **381**, 611
- Johnston S., Feain I. J., Gupta N., 2009, in Saikia D. J., Green D. A., Gupta Y., Venturi T., eds, Astronomical Society of the Pacific Conference Series Vol. 407, The Low-Frequency Radio Universe. p. 446 ([arXiv:0903.4011](https://arxiv.org/abs/0903.4011))
- Kaczmarek J. F., Purcell C. R., Gaensler B. M., Sun X., O'Sullivan S. P., McClure-Griffiths N. M., 2018, *MNRAS*, **476**, 1596
- Laing R. A., Bridle A. H., Parma P., Murgia M., 2008, *MNRAS*, **391**, 521
- Laing R. A., Bridle A. H., 2014, *MNRAS*, **437**, 3405
- Leahy J. P., Pooley G. G., Riley J. M., 1986, *MNRAS*, **222**, 753
- Leahy J. P., Black A. R. S., Dennett-Thorpe J., Hardcastle M. J., Komissarov S., Perley R. A., Riley J. M., Scheuer P. A. G., 1997, *MNRAS*, **291**, 20
- McNamara B. R., Nulsen P. E. J., 2012, *New Journal of Physics*, **14**, 055023
- Miller L., 1985, *MNRAS*, **215**, 773
- Morganti R., Fogasy J., Paragi Z., Oosterloo T., Orienti M., 2013, *Science*, **341**, 1082
- Mukherjee D., Bicknell G. V., Sutherland R., Wagner A., 2016, *MNRAS*, **461**, 967
- O'Sullivan S. P., et al., 2012, *MNRAS*, **421**, 3300
- O'Sullivan S. P., Purcell C. R., Anderson C. S., Farnes J. S., Sun X. H., Gaensler B. M., 2017, *MNRAS*, **469**, 4034
- Offringa A. R., de Bruyn A. G., Biehl M., Zaroubi S., Bernardi G., Pandey V. N., 2010, *MNRAS*, **405**, 155
- Reynolds J., 1994, ATNF Technical Memos, 39.3, 40
- Saikia D. J., Gupta N., 2003, *A&A*, **405**, 499
- Saikia D. J., Salter C. J., 1988, *ARA&A*, **26**, 93
- Sault R. J., Teuben P. J., Wright M. C. H., 1995, in Shaw R. A., Payne H. E., Hayes J. J. E., eds, Astronomical Society of the Pacific Conference Series Vol. 77, Astronomical Data Analysis Software and Systems IV. p. 433 ([arXiv:astro-ph/0612759](https://arxiv.org/abs/astro-ph/0612759))
- Schilizzi R. T., 1976, *AJ*, **81**, 946
- Schnitzeler D. H. F. M., et al., 2013, ATNF Technical Memos, 39.9, 129
- Sokoloff D. D., Bykov A. A., Shukurov A., Berkhuijsen E. M., Beck R., Poezd A. D., 1998, *MNRAS*, **299**, 189
- Tashiro M., Makishima K., Kaneda H., 2000, *Advances in Space Research*, **25**, 751
- Véron-Cetty M. P., Véron P., 2001, *A&A*, **375**, 791
- Westerlund B. E., Smith L. F., 1966, Australian Journal of Physics, **19**, 181
- Wilson W. E., et al., 2011, *MNRAS*, **416**, 832
- Wright E. L., 2006, *PASP*, **118**, 1711